ACS APPLIED MATERIALS & INTERFACES

www.acsami.org

Research Article

Functionalized-MXene Thin-Film Nanocomposite Hollow Fiber Membranes for Enhanced PFAS Removal from Water

Tin Le, Elnaz Jamshidi, Majid Beidaghi, and Milad Rabbani Esfahani*

Cite This: *ACS Appl. Mater. Interfaces* 2022, 14, 25397−25408

Read Online

ACCESS | Metrics & More | Article Recommendations | Supporting Information

ABSTRACT: Due to adverse health effects and the broad sources of per- and polyfluoroakyl substances (PFAS), PFAS removal is a critical research area in water purification. We demonstrate the functionalization of thin-film composite (TFC) hollow fiber nanofiltration (HFN) membranes by MXene nanosheets during the interfacial polymerization (IP) process for enhanced removal of perfluorooctane sulfonic acid (PFOS) from water. A MXene-polyamide (PA) selective layer was fabricated on top of a polysulfone (PSF) hollow fiber support via IP of trimesoyl chloride (TMC) and a mixture of piperazine (PIP) and MXene nanosheets to form MXene-PA thin-film nanocomposite (TFN) membranes. Incorporating MXene nanosheets during the IP process tuned the morphology and negative surface charge of the selective layer, resulting in enhanced PFOS rejection from 72% (bare TFC) to more than 96% (0.025 wt % MXene TFN), while the water permeability was also increased from 13.19 (bare TFC) to 29.26 LMH/bar (0.025 wt % MXene TFN). Our results demonstrate that both electrostatic interaction and size exclusion are the main factors governing the PFOS rejection, and both are determined by PA selective layer structural and chemical properties. The lamella structure and interlayer of MXene nanosheets inside the PA layer provided different transport mechanisms for water, ions, and PFAS molecules, resulting in enhanced water permeability and PFAS rejection due to traveling through the membrane by both diffusions through the PA layer and the MXene intralayer channels. MXene nanosheets showed very promising capability as a 2D additive for tuning the structural and chemical properties of the PA layer at the permeability-rejection tradeoff.

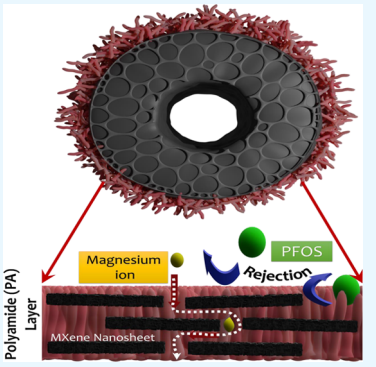

KEYWORDS: *MXene nanosheets, PFAS removal, per- and polyfluoroalkyl substances (PFAS), NF membrane, MXene−TFN membranes*

1. INTRODUCTION

Modern development within the past century has brought with it an explosive rise in water use and consumer goods. This has resulted in the contamination of water systems with various man-made chemicals. Per- and polyfluoroalkyl substances (PFAS) are a group of synthetic fluorinated compounds that come in a variety of sizes but are characterized by a hydrophilic head group and a hydrophobic tail.[1,2] The fluorine−carbon bonds that make up the tail also render PFAS difficult to break down, causing them to accumulate in the environment.[3] The primary source of PFAS contamination comes from household product manufacturing and military base exercises.[4] Despite the phasing out of many PFAS in manufacturing, the aftereffects are still being felt today, with PFAS being found within waterways in all 50 states and 97% of human blood samples.[5]

Efforts have been made to remove PFAS from water through methods such as adsorption[6] or membrane separation.[7−9] Studies on TFC membranes [reverse osmosis (RO) and nanofiltration (NF) membranes] show efficient PFAS rejection, with RO membranes being more effective (>99%) than NF membranes (>90%).[10] The lower pressure requirement for NF compared to RO makes NF a more economical and effective separation process if higher PFOS removal, near to that of RO, is achieved.[11] Due to the relatively high molecular weight (500.13 g/mol) and negative surface charge of PFOS, NF can retain PFOS based on size (steric) exculpation and electrostatic interaction.[12] In addition to the PFOS rejection capability of the NF membrane, water permeability (flux) of TFC membranes is an important factor controlling the separation efficiency at the permeability-rejection tradeoff. Both the rejection and permeability of TFC membranes depend on the structural and chemical properties of the PA layer, such as thickness, morphology, heterogeneity, and surface charge. Therefore, the development of novel NF membranes with functionalized and tuned PA selective layers that provide enhanced PFOS removal and enhanced permeability is of paramount importance to make NF an efficient and sustainable technology for water treatment. Wang et al.[13] used an NF TFC membrane (average pure water flux of 48 LMH) to reject both PFOS and perfluorobutane-

Received: March 1, 2022
Accepted: May 10, 2022
Published: May 24, 2022

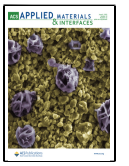

https://doi.org/10.1021/acsami.2c03796
ACS Appl. Mater. Interfaces 2022, 14, 25397−25408

sulfonic acid (PFBS) at 88.3 and 47.7%, respectively. It was found that size exclusion was the primary rejection mechanism for PFOS and electrostatic interaction for PFBS.[13] Similarly, Zhao et al.[14] used a commercial NF270 membrane to achieve 94.3% rejection of PFOS by size exclusion as well.[14] Although the size-exclusion mechanism has been identified as the primary mechanism for PFAS rejection, tuning the PA surface charge for enhanced electrostatic interaction will improve the rejection of negatively charged PFAS. Different surface functionalization techniques and materials, including polymers and 2D and 3D materials, have been used for functionalizing the PA selective layer.[15,16] Among the new generation of additives for membrane modification, MXenes have become particularly interesting 2D materials due to their high electrical conductivity, hydrophilicity, high specific area, and versatile chemistry.[17] They have shown promise in a variety of applications, including energy storage devices, batteries, supercapacitors,[18] interference shielding,[19] water desalination,[20] and separation membranes.[21]

MXenes are a large family of 2D transition metal carbides, carbonitrides, and nitrides with a general formula of $M_{n+1}X_nT_x$ (M represents transition metal, X is carbon/nitrogen, n can be 1 to 4, and T_x stands for different surface functional groups −OH, −O, and −F).[22] $Ti_3C_2T_x$, which is the MXene used in this study, is typically synthesized by etching Al layers from the structure of its parent MAX phase (Ti_3AlC_2).[22] MXene as two-dimensional (2D) nanosheets for membrane functionalization can provide nanochannels to the resultant membranes with longer diffusion routes for solute transport, enhance surface hydrophilicity due to the surface terminal functional groups, resulting in high water processability, enhance membrane chemical stability, facilitating membrane performance at extreme operational conditions, and enhance membrane selectivity by promoting higher negative surface charge to membrane surface.[23,24] $Ti_3C_2T_x$ implications for membrane fabrication showed promising results due to the appropriate water dispersity (an important factor for TFC fabrication), flexibility (an important factor for turnability of the PA layer), and physical−chemical stability (an important factor for the operation) of $Ti_3C_2T_x$.[25,26] Alfahel et al.[27] fabricated an MXene/cellulose acetate (CA) forward osmosis membrane as an alternative to commercial TFC FO membranes. With the addition of 8 wt % MXene, there was a 25% increase in water permeability compared to the bare CA membrane and enhanced fouling resistance, losing only 11% flux versus 32% flux decline for commercial membranes.[27] Zarshenas et al.[28] utilized MXene to create an RO thin-film nanocomposite (TFN) membrane by coating MXene with tannic acid and then incorporating 0.008 wt % onto PA TFC membranes. This resulted in an enhancement in permeability (40% higher) and antifouling (11% higher flux recovery ratio) compared to that of the bare TFC membrane.[28]

In this study, we demonstrate the fabrication of MXene−TFN membranes on a hollow fiber support tailored for enhanced PFOS rejection and water permeability. The performance of the fabricated MXene−TFN membranes for salt and PFOS removal was evaluated and compared to that of bare TFC NF membranes. The selective PA layer for the MXene−TFN membrane was extensively characterized to understand the relationship between the membrane performance in terms of PFOS removal, salt removal, water permeability, and antifouling and the changes in the physicochemical properties of the selective layer induced by the addition of MXene nanosheets.

2. MATERIALS AND METHODS

2.1. Materials and Chemicals. Polysulfone (Solvay Advanced Polymers), polyvinylpyrrolidone (Mpbio), and dimethylacetamide (VWR, HPLC grade) were used for the fabrication of hollow fiber support layers. Piperazine (Alfa Aesar, 99%), trimesoyl chloride (TCI, >98.0%), and n-hexane (Beantown Chemical, 95.0% min) were used for interfacial polymerization (IP) of the PA selective layer. Titanium powder (325 mesh, 99.5%, Alfa Aesar), aluminum powder (325 mesh, 99.5%, Alfa Aesar), graphite powder (325 mesh, 99% Alfa Aesar), lithium fluoride (325 mesh, 98.5% Alfa Aesar), and hydrochloric acid (36.5−38%, ACS grade, BDH) were used for the fabrication of the MAX phase.

2.2. Synthesis of the Ti_3AlC_2 MAX Phase. The Ti_3AlC_2 MAX phase was synthesized by mixing titanium (325 mesh, 99.5%, Alfa Aesar), aluminum (325 mesh, 99.5%, Alfa Aesar), and graphite (325 mesh, 99%, Alfa Aesar) powders in a 2:1:1 molar ratio, and the mixture was ball-milled for 18−24 h using zirconia balls. The mixture was then put into an alumina crucible and heated in a high-temperature furnace at 5 °C/min rate to 1400 °C and kept for 4 h. After cooling to room temperature, the obtained material was milled and crushed into powder and sieved to produce powders with a particle size of <38 μm.

2.3. Synthesis of $Ti_3C_2T_x$ MXenes. The $Ti_3C_2T_x$ MXenes were synthesized by etching Ti_3AlC_2 in a solution of HCl and LiF. First, a 9 M HCl solution was made by diluting concentrated HCl with DI water (40 mL total). Then, 3.2 g of LiF was added to the solution and stirred for 10 min with a magnetic bar to completely dissolve the salt. After totally dissolving LiF in HCl solution, 2 g of Ti_3AlC_2 was slowly added to 40 mL of the etchant over a period of 10 min to avoid rapid heat generation to the exothermic reaction. The mixture was then stirred continuously for 24 h at 35 °C. MXene powder was washed with repetitive steps of the centrifuge (3500 rpm for 5 min), handshaking the solutions for 2 min, and decantation of the supernatant until a dark green supernatant (pH > 5) was noticed. The delaminated MXene solution was then centrifuged at 3500 rpm for 1 h to separate the single-layer MXene flakes from multilayer MXene and unreacted MAX phase.

2.4. Hollow Fiber Membrane (Support Layer) Fabrication. Hollow fiber PSF ultrafiltration membranes were fabricated by the phase inversion technique. A polymer casting solution was created by adding 20 g PSF and 3 g PVP40 to 77 g DMAc. This mixture was mixed at room temperature overnight and allowed to rest for 4 h in order for bubbles to settle out of the solution. NF membranes were fabricated by a dry-wet spinning process using a 2 channel syringe pump (Chemyx) using 100 mL of DI water and 50 mL of casting solution; the polymer was doped at 2.5 mL/min, while the water acted as the boring solution at 1.5 mL/min.[29] The fabricated HFM were stored in DI water at 4°.

2.5. MXene-TFN NF Membrane Fabrication. TFC NF membranes were fabricated by forming a PA selective layer on top of the PSF hollow fiber support membranes via IP, as shown in Figure 1. PIP (2 g) was added to 98 g of DI water (aqueous phase) and stirred for 1 h. In this step, different amounts of MXene nanosheets (0.001, 0.005, 0.025, and 0.050 wt %) were added to the aqueous phase and stirred for 1 h. TMC (0.2 g) was added to 100 mL n-hexane and stirred for 1 h. For IP reaction, the HF PSF support membranes were immersed in the PIP solution for 2 min. Using an air knife, the excess solution was cleaned off. Next, the monomer-saturated HF support membrane was then dipped in TMC solution for 1 min, resulting in the formation of a thin-film composite (TFC) PA layer. The TFC membranes were then air-dried for 2 min before rinsing in DI water and then stored in DI water at 4 °C.[30] The blank (bare) TFC membranes were fabricated as explained above except that the addition of MXene into the aqueous phase was omitted.

2.6. MXene Nanosheet Characterization. Malvern Zetasizer Nano-ZS ZEN 3600 (Malvern Panalytical, Malvern, United King-

https://doi.org/10.1021/acsami.2c03796
ACS Appl. Mater. Interfaces 2022, 14, 25397−25408

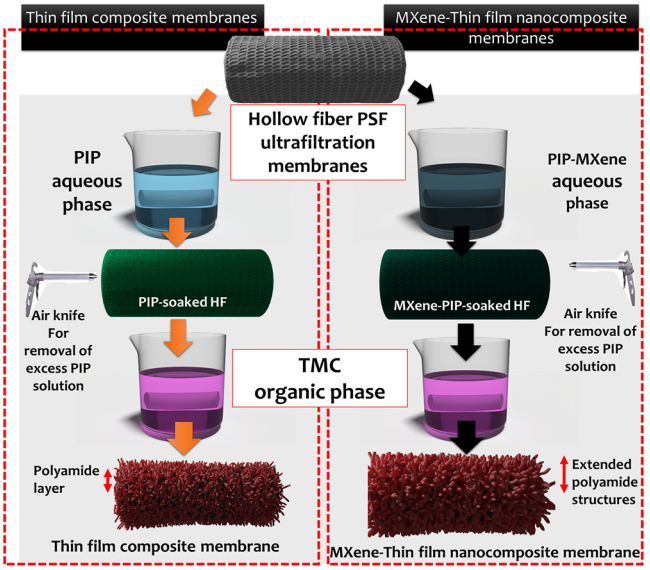

Figure 1. Fabrication of hollow fiber membranes by interfacial polymerization. The porous hollow fiber support layer was immersed in the aqueous phase (PIP) for 2 min. Then, the excess PIP solution was removed using an air knife. Next, the monomer-saturated HF support membrane was then dipped in TMC solution for 1 min, resulting in the formation of a TFC PA layer. The TFC membranes were then air-dried for 2 min before rinsing in DI water and then stored in DI water at 4 °C. The exact process was employed to fabricate MXene−TFN membranes by adding a certain amount of MXene nanosheets to the well-dispersed aqueous phase.

dom) was used to measure the zeta potential and the particle size distribution of the suspended MXene nanosheets. The size and thickness of the produced $Ti_3C_2T_x$ flakes were measured using an AFM (Park Systems, NX10, Suwon, South Korea). FTIR (Spectrum Two FT-IR Spectrometer with ATR, PerkinElmer, Waltham, United States) was used to investigate the functional surface groups of MXene. X-ray diffraction (XRD) experiments were performed using a powder diffractometer (Rigaku, SmartLab, Tokyo, Japan). By utilizing Bragg's law, the interlayer spacing of the MXene layers was calculated by the following equation[31]

$$d = \frac{\lambda}{2 \sin \theta} \tag{1}$$

where d is the interlayer spacing, λ is the radiation wavelength, and θ is the angle of an incident between the beam and the reflecting plane.

2.7. Membrane Characterization. XRD (Bruker D8, Billerica, United States) was used to characterize the fabricated membranes and determine the successful functionalization of MXene nanosheets within the PA layer. AFM (Dimension 3100, Veeco Digital Instruments, Plainview, United States) was used to measure the RMS surface roughness of membrane samples and determine the effect of MXene nanosheets on PA layer formation. The zeta potential of the membrane surface was evaluated by a streaming potential analyzer utilizing an adjustable gap cell (SurPASS 3, Anton Paar, Graz, Austria) as described elsewhere.[32] Measurements were performed with a solution containing 0.01 M KCl. Electrolyte solution flows into the cell were generated by pressure ranging from 600 to 200 mbar driven by a pump. The induced streaming potential was measured using Ag/AgCl electrodes mounted at each end of the adjustable gap cell.

The carboxylic group density of the polyamide selective layer was measured using the silver elution method.[33] The membranes were immersed for 10 min in 10 mL of 40 μM silver nitrate at 7 pH, twice to bind silver ions. Then, the excess silver ions were rinsed by four washes in 10 mL of 1 μM silver nitrate for 7 min. Finally, the membranes were immersed in 5 mL of 2% nitric acid for 30 min to elute the bound silver ions. ICP-OES (Optima 8300, PerkinElmer, Waltham, United States) was used to quantify silver ion concentration in the solution. The silver concentration was then converted to carboxyl group areal density using the following equation

$$[\mathrm{R} - \mathrm{COO}^-] = \frac{C_{\mathrm{Ag}+}\, V_{\mathrm{Ag}+} N_{\mathrm{A}}}{A} \tag{2}$$

where $[\mathrm{R{-}COO^-}]$ is the ionized carboxyl group areal density, A is the projected surface area of the polyamide film, C_{Ag^+} is the silver ion

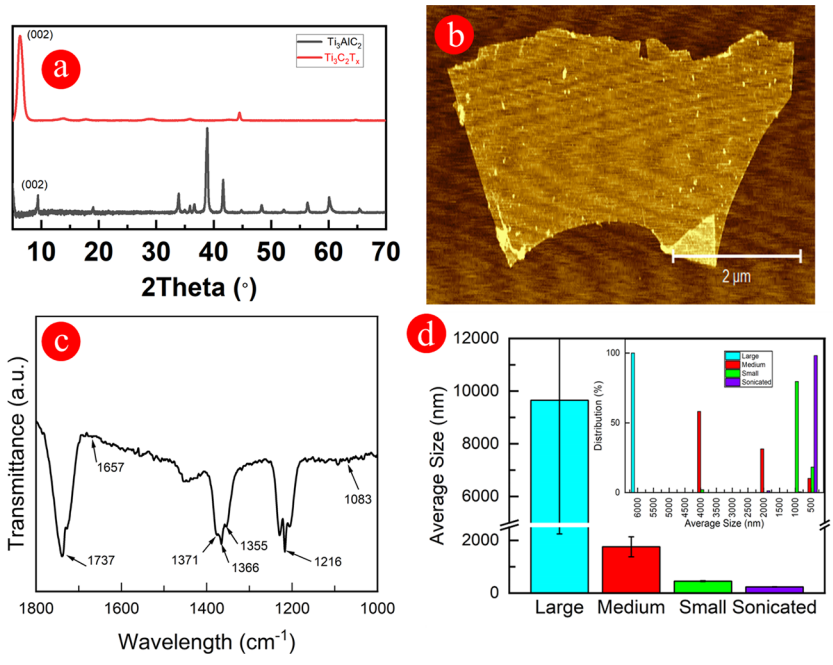

Figure 2. (a) XRD diffraction of MAX phase Ti_3AlC_2 and MXene film. (b) AFM image of a single MXene nanosheet. (c) FTIR spectra of MXene nanosheets. (d) particle size distribution of MXene nanosheets. Reported values correspond to the average of triplicate size measurements. Error bars represent the standard error of the mean.

https://doi.org/10.1021/acsami.2c03796
ACS Appl. Mater. Interfaces 2022, 14, 25397−25408

concentration, V_{Ag^+} is the elution volume, and N_A is Avogadro's number.[33] SEM (JEOL 7000 FE, Tokyo, Japan) was used to image the top surface morphology as well as the cross- section of fabricated membranes in order to examine the pore structures of the support layer and the morphology of the selective layer. ATR-FTIR (Spectrum 2, PerkinElmer, Waltham, United States) spectra were measured utilizing 8 scans from 450 to 4000 cm^{-1} at 4 cm^{-1} resolution, which were then averaged. The membrane was pressed against the crystal, PA layer down, and two replicates were measured. A background correction was performed on the spectra.[34] Water contact angles were measured utilizing a goniometer (Attension Theta Lite, Biolin Scientific, Uusimaa, Finland) by the sessile drop method. The hollow fiber membranes were flattened and a 4 μL water drop was dropped onto a random location and recorded for 10 s. This was repeated at a minimum of 5 other locations on the membrane, and this measurement was repeated for 3 different samples before averaging the data.

2.8. Membrane Performance and Salt and PFOS Rejection Tests. Prior to testing, the membranes were compacted at 70 psi for 90 min using DI water until there was no variation in permeate flux. The feed solution temperature was kept constant at 25.0 ± 0.5 °C throughout the experiment. After compacting, the membrane pure water permeance was measured at 65 psi for 60 min. Salt rejection of membranes was evaluated using a feed solution (2000 ppm $MgSO_4$) at 65 psi. PFOS rejection of membranes was evaluated using feed solutions containing 2 mg/L of PFOS in DI water. The rejection performance of NF membranes was determined by comparing the targeted species concentration in the feed (C_f) and permeate (C_p) based on the equation $R = 1 - C_p/C_f$. The membrane flux recovery ratio was evaluated based on the DI water flux before and after PFOS flux experiment and cleaning of membranes with DI water as explained here.[35] The salt concentrations in the feed and permeate were measured using a calibrated conductivity meter (Orion Star A212, Thermo Fisher, Waltham, United States). The PFOS concentration was determined using an ultrahigh-performance liquid chromatography (UPLC, Agilent I-class System) coupled with a mass spectrometer (Waters Xevo G2-XS Q-TOF MS). A sample volume of 1 μL was injected into a BEH C18 column (ACUITY UPLC, 1.7 μm, 2.1 × 50 mm) with a BEH C18 VanGuard Pre-Column (ACQUITY UPLC, 1.7 μm, 2.1 × 5 mm) using a mobile phase gradient of a solvent comprising 45% acetonitrile and 55% water with 20 mM ammonium acetate at a flow rate of 0.3 mL min^{-1}. The Q-TOF MS was operated using an electrospray ionization (ESI) interface in the negative mode. Samples (50 μL) were prepared using 5 ppm C^{13} PFOS isotope as an internal standard (IS) at a 9:1 sample/IS ratio. In addition, the stability (leaching) of the added MXene in the PA layer was examined under two conditions of static (no pressure and flow) and dynamic (65 psi filtration). The static test was completed by immersing the MXene−TFN membranes in DI water for 3 months and testing the possible leaching of MXene using ICP-OES. The dynamic leaching tests were done by measuring the MXene concentrations in the permeate of MXene−TFN membranes after 48 h filtration under 65 psi using DI water.

3. RESULTS AND DISCUSSION

3.1. Characterization of Synthesized MXene Nanosheets. Figure 2a shows the X-ray diffraction (XRD) patterns of the synthesized Ti_3AlC_2 MAX phase and a pristine MXene film fabricated by the vacuum filtration of a $Ti_3C_2T_x$ dispersion. The characteristic (001) peak of MXene appeared in the XRD pattern of the MXene film and showed that the (002) peak had shifted from ∼9.41° to a lower angle of ∼6.29° after etching. The absence of the main MAX phase at ∼39° in the XRD pattern of the MXene confirmed a near-complete etching of aluminum and the successful synthesis of MXene. The *d*-spacing of the MXene layers was determined to be 1.404 nm, which, with a single-layer thickness of 1 nm, resulted in an interlayer spacing of 0.404 nm, which is smaller than the Stokes radius of PFOS molecule (0.63 nm).[36,37] Figure 2b shows an atomic force microscopy (AFM) image of single-layer $Ti_3C_2T_x$, with a flake size of 0.2 μm on average. As shown in Figure 2b, all $Ti_3C_2T_x$ flakes have the same thickness of 1.0 nm and are characterized as monolayers. The FTIR spectra of MXene showed two typical representative peaks at 1657 and 1737 cm^{-1}, assigned to the vibration of the O functional group, OH at around 1371 and F at 1083 cm^{-1}. The size of MXene nanosheets is an important factor as the existence of particle sizes larger than the PA thickness might result in a defect PA layer. The size of MXene nanosheets is a function of the preparation method; specifically, the number of washing steps, shaking time, and centrifugation (speed and time) because larger flakes are more prone to delamination as interlayer bonds are weakened.[38]

Figure 2d shows that as the number of washes [defining a "wash" as a single handshaking and centrifuging cycle (for 60 min at 3000 rpm) of the MXene suspension (sediments and supernatant)] increased, the average particle size of MXene nanosheets decreased. In addition, the 10 min ultrasonication of MXene nanosheets after washing resulted in smaller nanosheets.[22] The ultrasonication not only reduced the average particle size but also increased the uniformity of the dispersion, as shown in the inset (Figure 2d). The smallest and the most uniform sample of MXene nanosheets was used to functionalize TFC membranes. Another critical factor in the immobilization of MXene nanosheets in the PA layer during the IP process is the position of the MXene nanosheet. Based on the size measurement, the average length of the MXene nanosheets was less than 500 nm with a thickness of 1 nm. If MXene nanosheets are positioned vertically with respect to the support layer, their larger size in comparison to the PA thickness generates defects in the PA layer. However, if MXene nanosheets are positioned horizontally during the IP process, the PA layer is formed around them by covering MXene nanosheets on top and bottom. Due to MXene nanosheet aspect ratio and van der Waals interlayer interactions between nanosheets, MXene nanosheets should be positioned in horizontal orientations in lamellar-like structures on the surface of the support layer during the PA formation.[39] Although there is a possibility of MXene nanosheet agglomeration due to van der Waals forces and high surface tension during the IP process, these nanosheets remain significantly thinner than the PA layer, with each sheet having an average thickness of around 1 nm.[40,41]

3.2. Polyamide Selective Layer Characteristics. In the formation of a PSF support layer, macrovoids were developed on both the inside and the outside boundary (Figure 3a), due to the instantaneous demixing of the casting solution and nonsolvent from both sides during the dry−wet spinning process.[42] Figure 3a also shows the presence of a fabricated PA selective layer on the outer surface of the hollow fiber support layer. The PA layer is fabricated on the surface of the support layer soaked in an amine solution (PIP) after contacting the acid chloride (TMC) in the organic solvent (hexane). The amine and acid chloride react at the aqueous−organic interface by the diffusion of amine from the aqueous phase to the organic phase. The PA layer formation includes rapid (tens of nanometers within seconds) formation of the incipient film followed by slow (tens of nanometers in minutes) growth of PA.[43] The growth of PA layer is limited by the diffusion of fresh (not yet reacted) amine from the aqueous phase to the organic phase through the already formed dense PA layer.[44−46]

https://doi.org/10.1021/acsami.2c03796
ACS Appl. Mater. Interfaces 2022, 14, 25397−25408

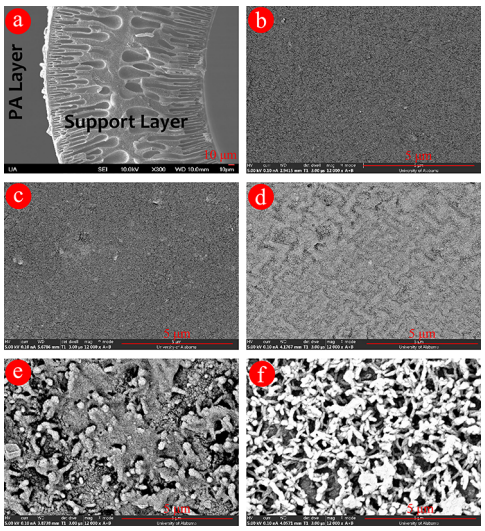

Figure 3. SEM images of the cross section of the (a) TFC membrane, the top surface of the (b) TFC membrane, (c) 0.001% MXene, (d) 0.005% MXene membrane surface, (e) 0.025% MXene, and (f) 0.050% MXene. The cross section is magnified at 300×, while the top surface images are magnified at 12,000×.

Therefore, the amount of PIP at the reaction interface determines the structure of the PA layer.

In general, the two preparation steps, including the absorbed PIP by the support layer (during the soaking process) and the amount of removed excess PIP (by and air-knife, roller, etc.), determine the quantity of PIP available for the IP process. The addition of hydrophilic MXene nanosheets into the PIP aqueous phase might facilitate providing more PIP transport into the interface reaction zone, resulting in lower PIP diffusion limitation and, therefore, the formation of an extended PA layer. In addition, the MXene nanosheets might have affected the partition coefficient of PIP into the organic phase, resulting in enhanced diffusion.[47] Figure 3b shows the top surface (PA selective layer) of the bare membrane with the nodular structure, which is the typical structure of the PA layer of the NF membrane. As the MXene loading inside the PA increased, the surface morphology of the PA layer changed from nodular structures in bare TFC to the elongated mega-nodule structures with enhanced heterogeneity at higher concentrations (Figure 3f).[48] At higher concentrations of MXene (0.025−0.050%), dark regions began to form, which could be a sign of agglomeration of MXene nanosheets. The support layer properties such as pore size and porosity and amine diffusion at the aqueous−organic interface determine the morphology and structure of the PA layer.[49] In general, smaller support pore sizes lead to increased PA film heterogeneity due to greater nanobubble (CO_2) confinement. The reaction between PIP and TMC in the IP process generates heat and HCl (strong acid) as a byproduct, which results in the reduction of dissolved gasses such as CO_2 and therefore the degassing of CO_2 during the IP process (Figure S1). The released small bubbles of CO_2 would be encapsulated as voids (nodules) in the cross-linked polyamide.[50] The enhanced surface heterogeneity of the MXene−TFC membrane can be explained due to the existence of MXene nanosheets acting as the thick layer confining CO_2 nanobubbles generated during the IP, resulting in mega-nodules. Figure 4 depicts the effects that MXene nanosheets in the aqueous phase have on the formation of polyamide during

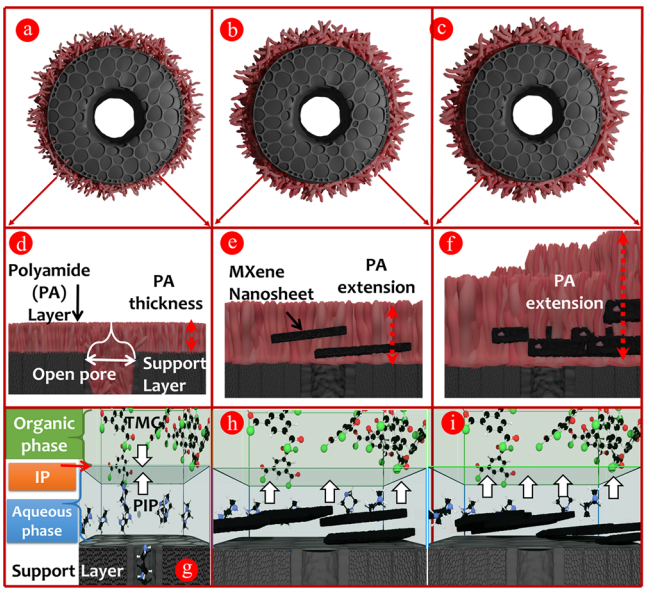

Figure 4. Schematic of hollow fiber TFN membranes with PSF support layer and (a) bare PA selective layer, (b) low-concentration MXene-PA selective layer, and (c) high-concentration MXene-PA selective layer. (d) Schematic of bare PA structure on the support layer showing the regular nodular structure with specific thickness and formation inside a pore of the support layer, (e) schematic of low-concentration MXene-PA structure on the support layer with extended structure and formation on the support layer, and (f) schematic of high-concentration MXene-PA structure on the support layer with elongated mega-nodule structures and enhanced heterogeneity. Schematic of interfacial polymerization (IP) showing (g) the interaction of aqueous phase (PIP) with organic phase (TMC) for bare TFC, (h) the interaction of aqueous phase (PIP + low concentration MXene) with organic phase (TMC) with promoted PIP transport from the support layer pore toward the interaction interface, and (i) the interaction of aqueous phase (PIP + high concentration MXene) with organic phase (TMC) with enhanced promoted PIP transport from the support layer pore toward the interaction interface. Atomic elements are represented by: black—carbon, blue—nitrogen, white—hydrogen, green—chlorine, red—oxygen.

interfacial polymerization. Figure 4d shows that for bare TFC, PIP in the aqueous phase enters the pores of the support, leading to the formation of PA inside the pores, which limits water transport through the support layer. When MXene nanosheets are added to the aqueous phase, in Figure 4e, due to their hydrophilic nature, they promoted the PIP transport toward the IP reaction interface, causing more PA to form on the surface rather than inside the pores, which possibly enhances the water permeability due to the alleviated mass transport resistance. However, as seen in Figure 4e, the higher amount of MXene resulted in agglomeration on the surface of the support layer, acting as dense films blocking the pores with PIP inside them and therefore preventing the formation of PA inside and on the mouth of the pore.[49] EDAX measurement, shown in Figure S4, displays MXene nanosheets in the PA layer, indicating successful functionalization of the outer selective layer.

Figure 5a shows a broad triple peak at 25, 30, and 35° for the bare TFC membrane corresponding to semi-crystalline monoclinic phases (α), which were shifted right, indicating a more compressed lattice.[51,52] The polyamide and polysulfone layers were highly amorphous, which prevented the appearance

https://doi.org/10.1021/acsami.2c03796
ACS Appl. Mater. Interfaces 2022, 14, 25397−25408

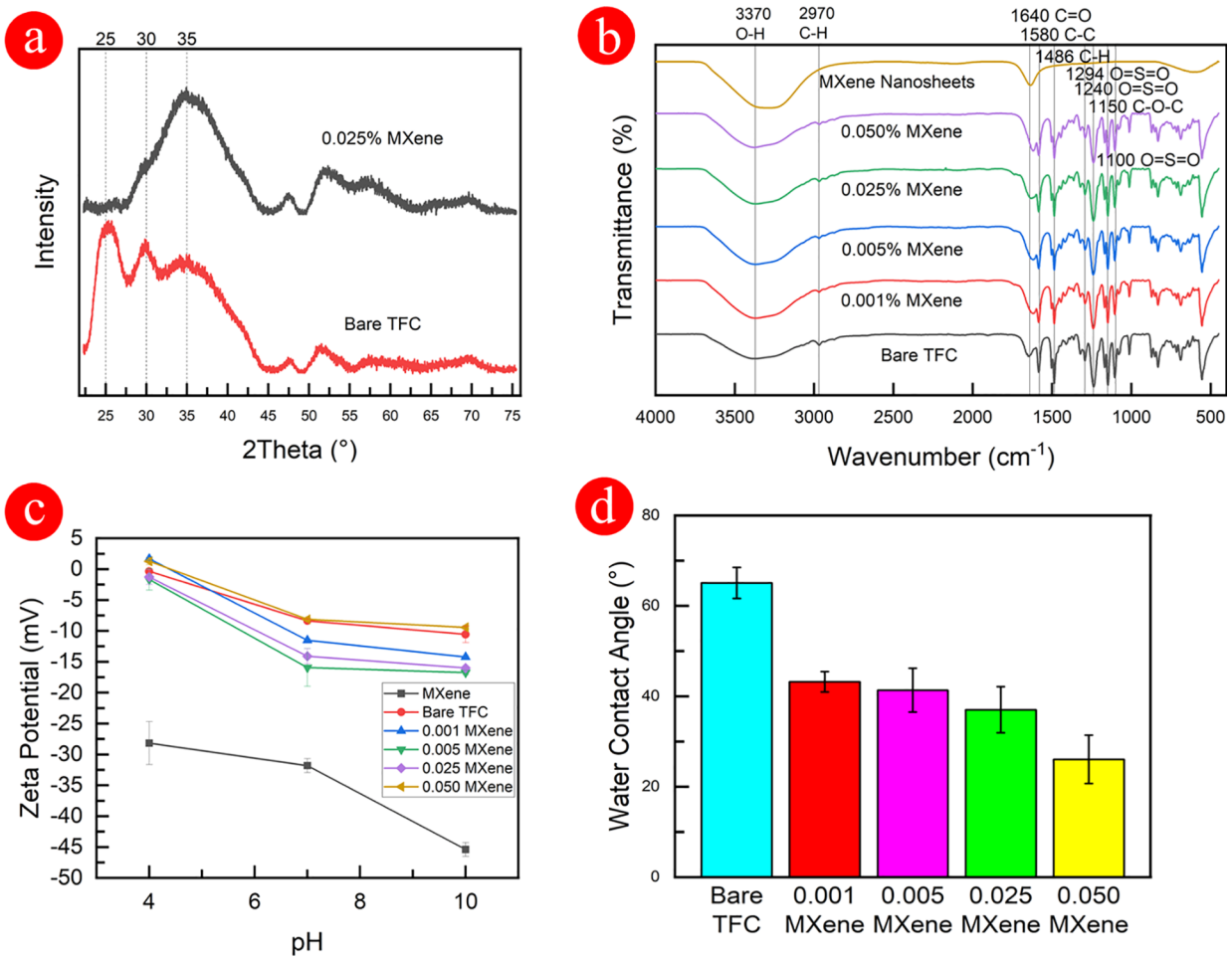

Figure 5. Membrane characterization showing (a) XRD pattern, (b) FTIR spectra, (c) surface zeta potential, and (d) water contact angle of TFC and MXene−TFC membranes. Reported values correspond to the average of triplicate size measurements. Error bars represent the standard error of the mean.

of sharp peaks.[53] The addition of 0.050% MXene loading resulted in the formation of a single broad peak at 35°, corresponding to the (104) plane, while the remaining peaks remained unchanged, indicating that surface functionalization did not significantly alter the membrane crystal structure.[54] The FTIR spectra for all samples are shown in Figure 5b. The broad peak at 3370 cm^{-1} is due to the absorption of water. There is an additional peak at 2970 cm^{-1} for all membranes that can be attributed to −CH groups. A peak at 1640 cm^{-1} is due to −C═O stretch forms. The peaks at 1580, 1486, 1294, 1240, 1150, and 1100 cm^{-1} correspond to C−C, C−H, O═S═O (symmetric), O═S═O (symmetric), C−O−C, and O═S═O (asymmetric) in the PSF support layer.[51] MXene spectra show peaks at 3350 and 1640 cm^{-1}.[36] The addition of MXene nanosheets did not significantly affect the spectra of TFC−MXene membranes, which may indicate the non-covalent interaction of MXene with the membrane.[55] The MXene−TFN membranes showed an increase in intensity for the 1640 cm^{-1} peak due to the addition of MXene nanosheets. Due to a combination of the low concentration of MXene used and the high penetration of the FTIR detecting the PSF support layer, more explicit MXene peaks were not visible.[28]

As shown in Figure 5c, all membranes showed more negative surface charge at basic pH. This behavior occurs due to the accumulation of H^+ ions, causing the surface charge to become less electronegative.[56] The PA selective layer inherently possesses an electronegative charge due to carboxyl groups from the hydrolysis of acyl chlorides from TMC.[7] The point of zero charge for the bare polyamide selective layer was determined to be around pH = 4 in agreement with reported data in the literature.[57] The MXene nanosheets were electronegatively charged across acidic, basic, and neutral environments.[58] It should be reminded that PFOS molecules are negatively charged due to sulfonic acid functional groups (Figure S2).[59]

Due to their higher electronegative charge of MXene-TFN compared to bare TFC at every pH, the functionalization of MXene nanosheets onto the PA selective layer would result in the enhancement of the electrostatic interactions of the TFC membrane.[41] The TFC-0.005 MXene membranes showed the most enhanced negative surface charge among the membranes with more than 3 times higher negative surface charge than bare TFC. However, the addition of a more-than-optimal concentration (>0.025) of MXene had no significant effect on the TFC membrane surface charge. This could be attributed to the agglomeration of MXene nanosheets on the surface, which hindered the effect of MXene nanosheets on the electrostatic charge of the TFC membrane.[60,61] By functionalizing the TFC membrane with MXene nanosheets, the water contact angle of the membrane was decreased as the MXene loading was increased (Figure 5d). The presence of many hydroxyl functional groups gives the MXene nanosheets a hydrophilic

https://doi.org/10.1021/acsami.2c03796
ACS Appl. Mater. Interfaces 2022, 14, 25397−25408

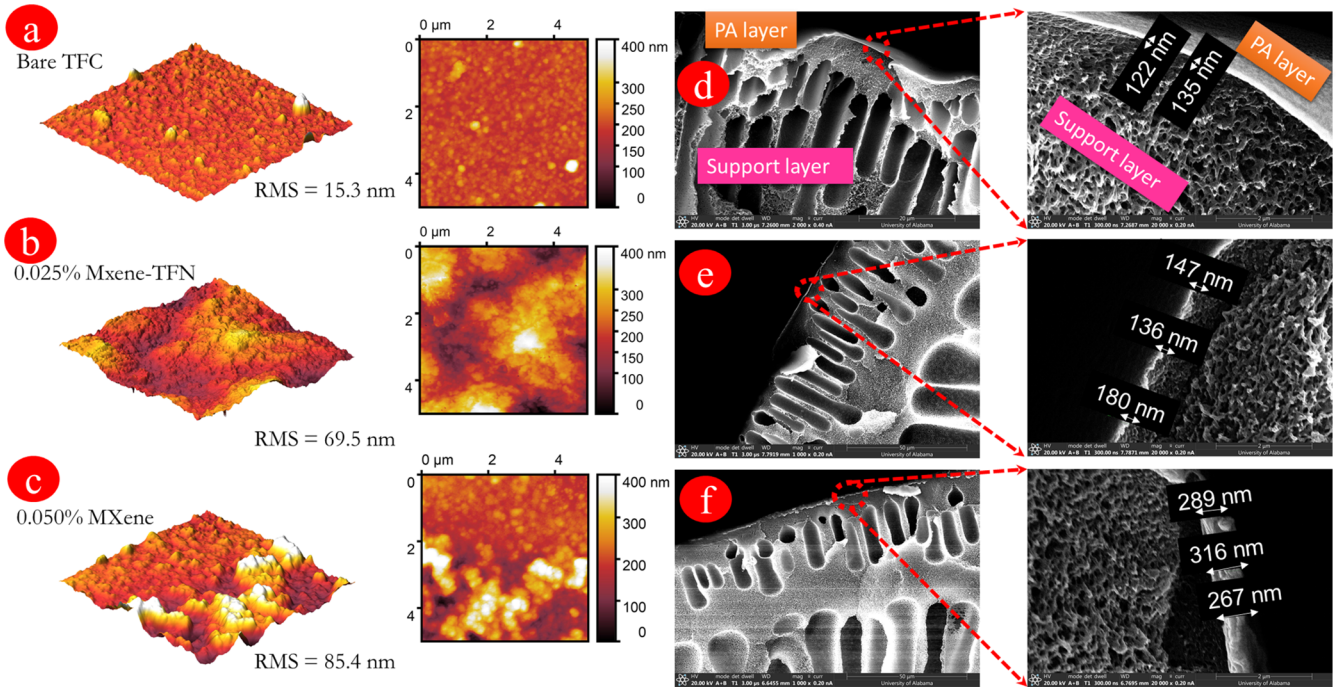

Figure 6. AFM images of (a) bare TFC, (b) 0.025 MXene−TFN, and (c) 0.050 MXene−TFN and SEM cross-sections of (d) bare TFC, (e) 0.025 MXene−TFN, and (f) 0.050 MXene−TFN. The AFM and SEM images show the enhanced surface roughness and thickness of the PA layer due to the incorporation of MXene nanosheets during the IP process.

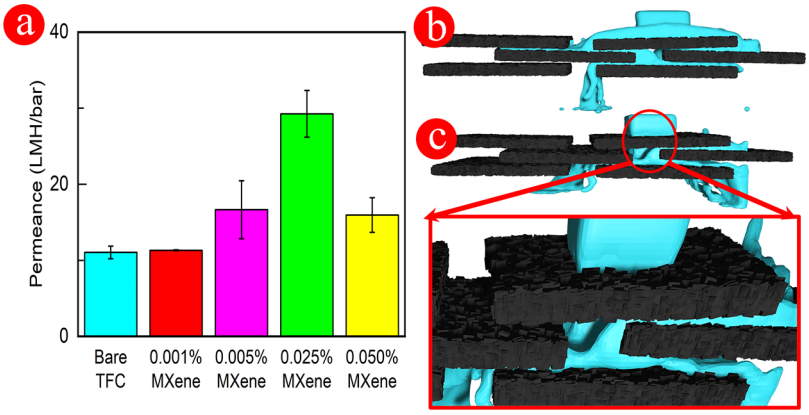

Figure 7. (a) Pure water permeance for bare TFC membranes and varying concentrations of MXene−TFN membranes. Membranes were compacted with DI H_2O feed for 1 h at 70 psi to reach constant flux; then, the permeate was collected at 65 psi for 1 h. Reported values correspond to the average of triplicate size measurements. Error bars represent the standard error of the mean. Schematic showing water transport pathways in (b) typical MXene nanosheets and (c) defect MXene nanosheets. A typical water transport pathway involves flowing through intralayer channels and between nanosheet gaps. However, defects and microvoids in the nanosheets may provide a quicker alternative to the main path, providing an increase in permeance.

nature, which allows their addition into the membrane to increase membrane surface hydrophilicity.[41,48] Another possible factor for the reduced contact angle of MXene−TFN is that the increased surface heterogeneity (Figure 3f) enhanced the surface hydrophilicity due to the presence of additional water channels for permeation. Following the Wenzel model, the already hydrophilic surface became more hydrophilic as the surface became rougher.[62−64]

AFM images and SEM cross sections (Figure 6) showed that as the MXene concentration increased, the membrane roughness increased significantly from RSM = 15.3 nm (bare TFC) to RSM = 85.4 nm for the 0.050% MXene−TFN membrane, and the average PA layer thickness was increased from 128.9 to 290.4 nm at the highest loading.

3.3. Membrane Flux. The pure water permeance of membranes with varying amounts of MXene loading was tested by cross-flow filtration at 65 psi. As shown in Figure 7, the addition of MXene enhanced the pure water permeance (PWP) from 13.19 to 29.26 LMH/bar (at 0.025% MXene), but as the MXene loading increased further, there was a decrease in PWP to 16.15 LMH/bar (which was still higher than PWP of bare TFC (13.19 LMH/bar). This behavior can be justified based on the fact that the addition of highly hydrophilic nanosheets into the PA layer enhanced the hydrophilicity of the membrane, resulting in enhanced water permeability.[41] Another reason for the enhanced water permeability of the MXene−TFN membrane compared to the bare TFC might be due to the position and morphology of

https://doi.org/10.1021/acsami.2c03796
ACS Appl. Mater. Interfaces 2022, 14, 25397−25408

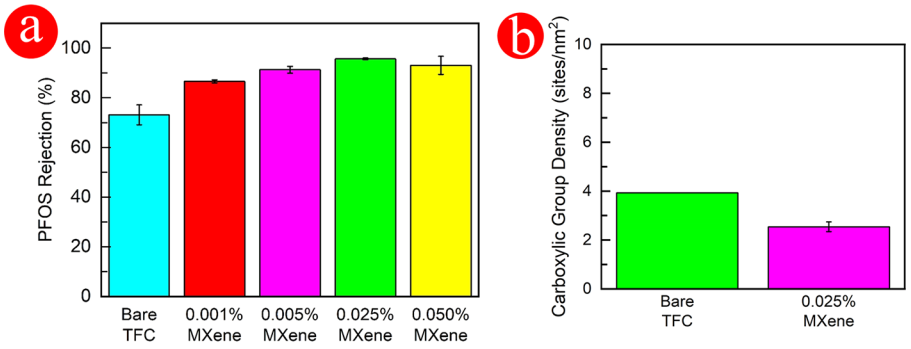

Figure 8. (a) PFOS rejection for bare TFC membranes and varying concentrations of MXene TFN membranes. The feed solution consists of 2 ppm PFOS solutions. The feed is run for 30 min, and then the permeate is collected for 10 min. Reported values correspond to the average of triplicate size measurements. Error bars represent the standard error of the mean. (b) Carboxylic group density of bare TFC and the optimal MXene loading.

the formed PA layer. The presence of hydrophilic MXene nanosheets in the aqueous phase during the IP process decreases the transport resistance of PIP to the organic phase during interfacial polymerization, shifting the formation of the PA layer from inside the pores of the support layer to the surface of support layer (Figure 4).

The formation of the PA layer on the mouth of pores, instead of inside the pores, reduces the water transport resistance inside the pores, resulting in enhanced water permeability.[48] In addition, another possible justification for the enhanced water permeability of MXene−TFN membranes is the presence of MXene nanosheets interfered with PA cross-linking, which generated defects.[48] The decrease in PWP, among the MXene−TFN membranes, at the highest MXene loading (TFN-0.050% MXene membranes) can be explained based on the stacking of MXene nanosheets inside the PA layer, which blocked water transport on the surface.[41] However, the permeance of TFC-0.050% MXene membranes remained 22% higher compared to bare TFC due to the higher hydrophilicity and structure of the PA layer. This behavior can be justified based on the lamellar structure formed by MXene nanosheets within the PA layer as one of the governing transport mechanisms (Figure 7b). In such a structure, the typical water transport pathway involves flowing through intralayer channels and between nanosheet gaps, resulting in long pathways. However, defects and microvoids in the nanosheets may provide a quicker alternative to the main pathway, providing an increase in permeance, as in shown in Figure 7c.[65] These defects may form during the MILD synthesis of MXenes due to HF etching.[66] As more layers are stacked, these defects can be blocked, possibly hindering water transport, as shown at the highest MXene loading.[65]

3.4. Rejection, Fouling, and Stability of Membranes.

The PFOS rejection of the membranes was measured to determine whether the MXene functionalization of the PA selective layer would result in improved PFOS rejection. In general, TFC−NF hollow fiber membranes fabricated by piperazine (PIP, MW of 86.1 g/mol) and TMC exhibit around 70% $MgSO_4$ rejection.[30] Rejection of charged solutes such as PFOS by electrostatic (Donnan) exclusion is directly related to the charge characteristics of the polyamide selective layer. Retention of PFOS by the NF membrane is determined by the coupled influence of the membrane pore size and charge and the physicochemical properties of PFOS. The PFOS rejection was evaluated using a feed solution containing 2 mg/L PFOS in DI water. Figure 8 shows that adding MXene significantly enhanced the PFOS removal from 78.9% bare TFC to 97.6 at 0.025% MXene loading. PFOS has a relatively high molecular weight of 500.13 g/mol, and the size exclusion should play a critical role in PFOS retention. In addition, at a solution pH of 5.5 (original pH, not adjusted), which was the tested membrane filtration condition, both the membranes and PFOS were negatively charged (Figure 5).

As shown in Figure 5c, the addition of highly electronegatively charged MXene nanosheets increased the electronegativity of the functionalized membranes, which facilitates surface repulsion of the negatively charged PFOS molecules.[41] Silver elution analysis revealed that the 0.025%-MXene−TFN membrane had significantly lower carboxyl group density (2.54 sites/nm^2 *vs* 3.93 sites/nm^2), which indicates a higher degree of cross-linking.[33] The silver elution analysis showed that the carboxylic group density was higher for bare TFC; however, as shown in Figure 5c, the 0.025%-MXene−TFN had a more negative zeta potential.[7] This higher negative surface charge is due to MXene nanosheets' inherent negative zeta potential having a more significant contribution to the membrane than that of carboxylic groups. Based on the discussed membrane characterization, the MXene-TFN membranes possessed a higher surface charge (Figure 5) and higher surface heterogeneity (extended) of the PA layer (Figure 5). Therefore, the enhanced PFOS removal due to the immobilization of MXene can be attributed to electrostatic repulsion followed by size selectivity. As discussed earlier, the MXene−TFN membranes possessed a larger extended structure of the PA selective layer due to the presence of MXene, which explains the enhanced PFOS rejection due to the extended thickness of the selective layer. These results emphasize that the structure and thickness of the PA selective layer, in addition to charge properties, control the ion rejection/selectivity of NF membranes. Further increasing the MXene concentration (0.050%) resulted in a negligible (4%) decrease in rejection compared to 0.025%-MXene−TFC membranes due to the agglomeration of MXene nanosheets resulting in defects in the PA layer.[67] Another explanation for the slight reduction of PFOS in the 0.050%-MXene−TFC membrane is their less electronegative surface charge, as explained earlier (Figure 5c).

Figure 9a shows the $MgSO_4$ salt rejection performance of the synthesized membranes. The salt rejection results showed that as the MXene concentration increased up to 0.025% MXene loading, there was an insignificant decrease (less than 4%) in $MgSO_4$ rejection. This trend of no significant reduction

https://doi.org/10.1021/acsami.2c03796
ACS Appl. Mater. Interfaces 2022, 14, 25397−25408

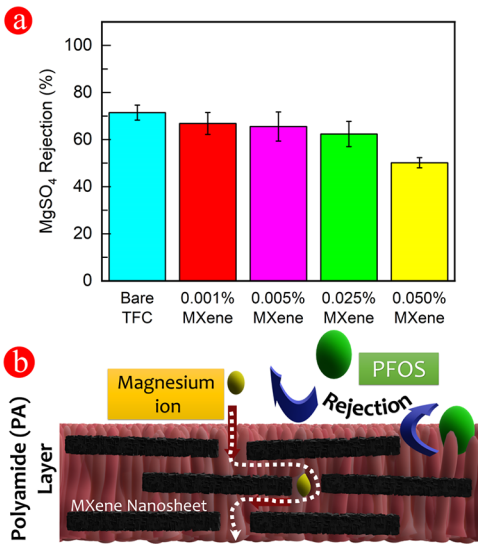

Figure 9. (a) Magnesium sulfate rejection for bare TFC membranes and varying concentrations of MXene−TFN membranes. The feed solution consists of 2000 ppm $MgSO_4$ solution. The feed ran for 30 min and permeate collected for 10 min under 65 psi pressure, pH = 5.5, and temperature 25 ± 0.5 °C. Reported values correspond to the average of triplicate size measurements. Error bars represent the standard error of the mean. (b) Schematic of rejection mechanism for TFN membrane toward $MgSO_4$ and PFOS. The lamellar structure that was formed by MXene inside the PA layer resulted in interlayer spaces that swell when exposed to water during the filtration, resulting in passing $MgSO_4$ ions (0.35, 0.23 nm). However, the larger size of PFOS molecules (0.63 nm) prevented PFOS transport through MXene channels.

on the salt rejection of membranes while improving the membrane permeability (Figure 7) confirmed the successful functionalization of TFC membranes with MXene, where the incorporation of MXene to the PA layer increased the membrane permeability without sacrificing the salt rejection at the rejection-permeability tradeoff, while 97% PFOS rejection (improvement of more than 35% compared to bare TFC) was achieved (Figure 9a). Further increasing the MXene loading to 0.050% resulted in a decrease in $MgSO_4$ rejection. This behavior was also reported by other groups.[7,41,68] This phenomenon can be attributed to higher loading of MXene, causing a loose PA structure regarding salt rejection.[41]

During the IP process, the higher concentration of MXene nanosheets in the aqueous phase interacts with PIP by hydrogen bonding, which impedes interfacial polymerization, resulting in decreased PA cross-linking.[48] Therefore, the higher load of MXene in 0.050%-MXene−TFC membranes should have a lower cross-linked PA selective layer, resulting in lower salt rejection compared with other membranes. Additionally, the lamellar structure that was formed by MXene inside the PA layer resulted in interlayer spaces that swell when exposed to water during the filtration, resulting in a loss of salt rejection.[69] The negative surface charge of the MXene channels cause the cations to attach to each side of the intralayer channels, creating repulsive forces between cations that expand the interlayer channels.[48,68] This did not result in the loss of PFOS rejection as, unlike the $MgSO_4$ ions (0.35, 0.23 nm), the PFOS molecules (0.63 nm) were significantly larger than the interlayer channels (0.40 nm) (Figure 9b).[37,70] In addition, the negative surface charge of the MXene channels caused Mg^{2+} counterions to exhibit higher transport rates through the membrane. While the SO_4^- co-ions are slowed, the net increase in ion transport would result in a loss of salt rejection.[65]

As shown in Figure 10, the flux recovery ratio (FRR %) of the MXene−TFN membranes increased as the MXene loading

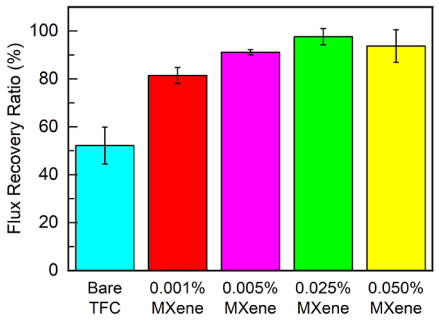

Figure 10. Flux recovery ratio (FRR %) for bare TFC membranes and MXene−TFN membranes. FRR % is the ratio between the pure water flux (J_{w1}) of virgin (not used) membrane and pure water flux (J_{w2}) after filtration of 2 ppm PFOS solution and 15 min of cleaning with pure water at atmospheric pressure. J_{w2} is measured after 30 min of cleaning with DI H_2O at 65 psi. Reported values correspond to the average of triplicate size measurements. Error bars represent the standard error of the mean.

increased to a maximum of 98% at 0.025% MXene loading. The enhanced (almost 100%) FRR ratio of 0.025%-MXene−TFN membranes shows no interaction or very weak physical interaction (deposition) between PFOS and the MXene-PA surface layer, which could be completely restored after washing with only DI water. In addition, 48 h PFOS filtration showed that 0.025%-MXene−TFN membranes showed no flux decline during the PFOS filtration, while the bare TFC membrane showed around 20% flux decline. This behavior indicates a lack of significant PFOS adsorption on 0.025%-MXene−TFN. Based on Figure 5c, this can be due to electrostatic interaction from the highly negatively charged MXene nanosheets repelling the negatively charged PFOS molecules.[41] In addition, the increased hydrophilicity of MXene−TFC membranes (Figure 5d) promoted the formation of a hydration layer on the surface of the membrane, which prevented severe attachment of PFOS on the membrane surface.[27] The 0.050% MXene−TFN membranes showed FRR % reduction compared to the 0.025% MXene−TFN membranes, which can be justified due to the higher surface roughness of the membrane, as shown in Figure 6.

These data represent the physical settlement of PFOS on the membrane surface with reversible fouling rather than adsorption or pore blocking fouling mechanism. In addition to the membrane performance (rejection, flux, and fouling), the stability of MXene inside the PA layer was tested under two conditions of static (under no pressure) and dynamic (filtration under 65 psi pressure). Figure S3 shows that for both 24 h dynamic conditions and 3 month static conditions, there was no significant leaching of MXene, indicating that the MXene−TFN was water-stable over long periods of time. The MXene nanosheets are bonded to the PA layer due to hydrogen bonding and van der Waals interactions as well as physical immobilization by the enhanced cross-linking density of the PA.[41] Although negligible, it was noticed that both static and dynamic leaching tests resulted in the same amount

https://doi.org/10.1021/acsami.2c03796
ACS Appl. Mater. Interfaces 2022, 14, 25397−25408

(0.4%) of MXene leaching, that is, those MXene nanosheets that did not bind with PIP during the IP process.

4. CONCLUSIONS

In this study, we reported the fabrication of a novel MXene–TFN hollow fiber NF membrane by using MXene nanosheets as the additives to the PA selective layer to enhance the removal of PFOS from water without sacrificing the salt rejection of membranes while enhancing the membrane flux. We were able to successfully functionalize the PA layer by incorporating MXene nanosheets into the aqueous phase during interfacial polymerization and tuning the surface charge and morphology of the PA layer for enhanced PFOS removal, while the water permeability of the membrane was also improved. The main factors promoting the enhanced PFOS removal were electrostatic repulsion and size selectivity due to the negative surface charge of MXene and enhanced extended nodular structure of PA due to the existence of MXene nanosheets during the IP process. In addition, results showed an optimum MXene loading at 0.025 wt % to achieve the enhanced PFOS rejection by over 20% (from 72 to 96%) compared to the bare TFC without any reduction in $MgSO_4$ rejection. The rejection data showed that the salt ions ($MgSO_4$) and PFOS molecules followed different transport mechanisms regarding the lamella structure and interlayer spacing of MXene nanosheets inside the PA layer. These results show the successful implication of MXene nanosheets as 2D additives for tuning TFC membrane properties toward the enhanced removal of emerging pollutants such as PFAS.

ASSOCIATED CONTENT

Supporting Information

The Supporting Information is available free of charge at https://pubs.acs.org/doi/10.1021/acsami.2c03796.

Interfacial polymerization chemical equation, zeta potential of PFOS, MXene leaching, and EDAX mapping of the 0.025- and 0.050-MXene polyamide layers (PDF)

AUTHOR INFORMATION

Corresponding Author

Milad Rabbani Esfahani − *Department of Chemical and Biological Engineering, The University of Alabama, Tuscaloosa, Alabama 35487, United States;* orcid.org/0000-0001-6530-4310; Phone: 205-348-8836; Email: mesfahani@eng.ua.edu

Authors

Tin Le − *Department of Chemical and Biological Engineering, The University of Alabama, Tuscaloosa, Alabama 35487, United States*

Elnaz Jamshidi − *Department of Mechanical Engineering, Auburn University, Auburn, Alabama 36849, United States*

Majid Beidaghi − *Department of Mechanical Engineering, Auburn University, Auburn, Alabama 36849, United States*

Complete contact information is available at: https://pubs.acs.org/10.1021/acsami.2c03796

Notes

The authors declare no competing financial interest.

ACKNOWLEDGMENTS

The authors gratefully thank the Chemical and Biological Engineering Department of the University of Alabama and the Alabama Water Institute of the University of Alabama. The authors acknowledge the support of the Department of the Interior (DOI) Bureau of Reclamation (BR) under agreement number R19AC00087, the United States Geological Survey (USGS) under grant number 20-WRC-207214, and the Environmental Protection Agency (EPA) under award number 84014501. The authors thank Ka Ming Law from Dr. Hauser Group, Department of Physics and Astronomy of the University of Alabama, for AFM imaging of membranes. The work performed at Auburn University was supported by a National Science Foundation grant (OAI-1929195).

REFERENCES

(1) Alves, A. V.; Tsianou, M.; Alexandridis, P. Fluorinated Surfactant Adsorption on Mineral Surfaces: Implications for PFAS Fate and Transport in the Environment. *Surfaces* **2020**, *3*, 516–566.

(2) Hu, X. C.; Andrews, D. Q.; Lindstrom, A. B.; Bruton, T. A.; Schaider, L. A.; Grandjean, P.; Lohmann, R.; Carignan, C. C.; Blum, A.; Balan, S. A.; et al. Detection of Poly- and Perfluoroalkyl Substances (PFASs) in U.S. Drinking Water Linked to Industrial Sites, Military Fire Training Areas, and Wastewater Treatment Plants. *Environ. Sci. Technol. Lett.* **2016**, *3*, 344–350.

(3) Hekster, F. M.; Laane, R. W. P. M.; de Voogt, P. Environmental and Toxicity Effects of Perfluoroalkylated Substances. *Rev. Environ. Contam. Toxicol.* **2003**, *179*, 99–121.

(4) Zhao, C.; Zhang, J.; He, G.; Wang, T.; Hou, D.; Luan, Z. Perfluorooctane sulfonate removal by nanofiltration membrane the role of calcium ions. *Chem. Eng. J.* **2013**, *233*, 224–232.

(5) Khalil, N.; Chen, A.; Lee, M.; Czerwinski, S. A.; Ebert, J. R.; DeWitt, J. C.; Kannan, K. Association of Perfluoroalkyl Substances, Bone Mineral Density, and Osteoporosis in the U.S. Population in NHANES 2009-2010. *Environ. Health Perspect.* **2016**, *124*, 81–87.

(6) Liu, L.; Liu, Y.; Gao, B.; Ji, R.; Li, C.; Wang, S. Removal of perfluorooctanoic acid (PFOA) and perfluorooctane sulfonate (PFOS) from water by carbonaceous nanomaterials: A review. *Crit. Rev. Environ. Sci. Technol.* **2020**, *50*, 2379–2414.

(7) Boo, C.; Wang, Y.; Zucker, I.; Choo, Y.; Osuji, C. O.; Elimelech, M. High Performance Nanofiltration Membrane for Effective Removal of Perfluoroalkyl Substances at High Water Recovery. *Environ. Sci. Technol.* **2018**, *52*, 7279–7288.

(8) Fetanat, M.; Keshtiara, M.; Keyikoglu, R.; Khataee, A.; Daiyan, R.; Razmjou, A. Machine learning for design of thin-film nanocomposite membranes. *Sep. Purif. Technol.* **2021**, *270*, 118383.

(9) Abdikheibari, S.; Baskaran, K.; Guijt, R.; Lei, W.; Dumée, L. F. Cross-linked boron nitride-piperazine amide thin film nanocomposite membranes for rejection and concentration of per- and polyfluoroalkyl substances (PFAS). *Environ. Qual. Manag.* **2022**, DOI: 10.1002/tqem.21828.

(10) Tang, C. Y.; Fu, Q. S.; Criddle, C. S.; Leckie, J. O. Effect of Flux (Transmembrane Pressure) and Membrane Properties on Fouling and Rejection of Reverse Osmosis and Nanofiltration Membranes Treating Perfluorooctane Sulfonate Containing Wastewater. *Environ. Sci. Technol.* **2007**, *41*, 2008–2014.

(11) Mohammad, A. W.; Teow, Y. H.; Ang, W. L.; Chung, Y. T.; Oatley-Radcliffe, D. L.; Hilal, N. Nanofiltration membranes review: Recent advances and future prospects. *Desalination* **2015**, *356*, 226–254.

(12) Luo, J.; Wan, Y. Effects of pH and salt on nanofiltration—a critical review. *J. Membr. Sci.* **2013**, *438*, 18–28.

(13) Wang, J.; Wang, L.; Xu, C.; Zhi, R.; Miao, R.; Liang, T.; Yue, X.; Lv, Y.; Liu, T. Perfluorooctane sulfonate and perfluorobutane sulfonate removal from water by nanofiltration membrane: The roles of solute concentration, ionic strength, and macromolecular organic foulants. *Chem. Eng. J.* **2018**, *332*, 787–797.

(14) Zhao, C.; Tang, C. Y.; Li, P.; Adrian, P.; Hu, G. Perfluorooctane sulfonate removal by nanofiltration membrane—the effect and interaction of magnesium ion / humic acid. *J. Membr. Sci.* **2016**, *503*, 31−41.
(15) Esfahani, M. R.; Aktij, S. A.; Dabaghian, Z.; Firouzjaei, M. D.; Rahimpour, A.; Eke, J.; Escobar, I. C.; Abolhassani, M.; Greenlee, L. F.; Esfahani, A. R.; et al. Nanocomposite membranes for water separation and purification: Fabrication, modification, and applications. *Sep. Purif. Technol.* **2019**, *213*, 465−499.
(16) Le, T.; Chen, X.; Dong, H.; Tarpeh, W.; Perea-Cachero, A.; Coronas, J.; Martin, S. M.; Mohammad, M.; Razmjou, A.; Esfahani, A. R.; et al. An Evolving Insight into Metal Organic Framework-Functionalized Membranes for Water and Wastewater Treatment and Resource Recovery. *Ind. Eng. Chem. Res.* **2021**, *60*, 6869−6907.
(17) Naguib, M.; Kurtoglu, M.; Presser, V.; Lu, J.; Niu, J.; Heon, M.; Hultman, L.; Gogotsi, Y.; Barsoum, M. W. Two-dimensional nanocrystals produced by exfoliation of Ti3 AlC2. *Adv. Mater.* **2011**, *23*, 4248−4253.
(18) Ghidiu, M.; Lukatskaya, M. R.; Zhao, M.-Q.; Gogotsi, Y.; Barsoum, M. W. Conductive two-dimensional titanium carbide 'clay' with high volumetric capacitance. *Nature* **2014**, *516*, 78−81.
(19) Shahzad, F.; Alhabeb, M.; Hatter, C. B.; Anasori, B.; Man Hong, S.; Koo, C. M.; Gogotsi, Y. Electromagnetic Interference Shielding with 2D Transition Metal Carbides (MXenes). *Science* **2016**, *353*, 1137−1140 Journal Article.
(20) Tong, X.; Liu, S.; Qu, D.; Gao, H.; Yan, L.; Chen, Y.; Crittenden, J. Tannic acid-metal complex modified MXene membrane for contaminants removal from water. *J. Membr. Sci.* **2021**, *622*, 119042.
(21) Ding, L.; Wei, Y.; Wang, Y.; Chen, H.; Caro, J.; Wang, H. A Two-Dimensional Lamellar Membrane: MXene Nanosheet Stacks. *Angew. Chem. Int. Ed.* **2017**, *56*, 1825−1829.
(22) Alhabeb, M.; Maleski, K.; Anasori, B.; Lelyukh, P.; Clark, L.; Sin, S.; Gogotsi, Y. Guidelines for Synthesis and Processing of Two-Dimensional Titanium Carbide (Ti3C2Tx MXene). *Chem. Mater.* **2017**, *29*, 7633−7644.
(23) Ren, C. E.; Hatzell, K. B.; Alhabeb, M.; Ling, Z.; Mahmoud, K. A.; Gogotsi, Y. Charge- and Size-Selective Ion Sieving Through Ti3C2Tx MXene Membranes. *J. Phys. Chem. Lett.* **2015**, *6*, 4026−4031.
(24) Kwon, O.; Choi, Y.; Kang, J.; Kim, J. H.; Choi, E.; Woo, Y. C.; Kim, D. W. A comprehensive review of MXene-based water-treatment membranes and technologies: Recent progress and perspectives. *Desalination* **2022**, *522*, 115448.
(25) Pandey, R. P.; Rasool, K.; Madhavan, V. E.; Aïssa, B.; Gogotsi, Y.; Mahmoud, K. A. Ultrahigh-flux and fouling-resistant membranes based on layered silver/MXene (Ti3C2Tx) nanosheets. *J. Mater. Chem. A* **2018**, *6*, 3522−3533.
(26) Xu, D.; Zhu, X.; Luo, X.; Guo, Y.; Liu, Y.; Yang, L.; Tang, X.; Li, G.; Liang, H. MXene Nanosheet Templated Nanofiltration Membranes toward Ultrahigh Water Transport. *Environ. Sci. Technol.* **2021**, *55*, 1270−1278.
(27) Alfahel, R.; Azzam, R. S.; Hafiz, M.; Hawari, A. H.; Pandey, R. P.; Mahmoud, K. A.; Hassan, M. K.; Elzatahry, A. A. Fabrication of fouling resistant Ti3C2Tx (MXene)/cellulose acetate nanocomposite membrane for forward osmosis application. *J. Water Proc. Eng.* **2020**, *38*, 101551.
(28) Zarshenas, K.; Dou, H.; Habibpour, S.; Yu, A.; Chen, Z. Thin Film Polyamide Nanocomposite Membrane Decorated by Polyphenol-Assisted Ti3C2Tx MXene Nanosheets for Reverse Osmosis. *ACS Appl. Mater. Interfaces* **2022**, *14*, 1838−1849.
(29) Mohammadi Ghaleni, M.; Al Balushi, A.; Bavarian, M.; Nejati, S. Omniphobic Hollow Fiber Membranes for Water Recovery and Desalination. *ACS Appl. Polym. Mater.* **2020**, *2*, 3034−3038.
(30) Xia, L.; Ren, J.; McCutcheon, J. R. Braid-reinforced thin film composite hollow fiber nanofiltration membranes. *J. Membr. Sci.* **2019**, *585*, 109−114.
(31) Sheng, Y.; Tang, X.; Peng, E.; Xue, J. Graphene oxide based fluorescent nanocomposites for cellular imaging. *J. Mater. Chem. B* **2013**, *1*, 512−521.
(32) Bukšek, H.; Luxbacher, T.; Petrinić, I. Zeta Potential Determination of Polymeric Materials Using Two Differently Designed Measuring Cells of an Electrokinetic Analyzer. *Acta Chim. Slov.* **2010**, *57*, 700−706. Journal Article
(33) Chen, D.; Werber, J. R.; Zhao, X.; Elimelech, M. A facile method to quantify the carboxyl group areal density in the active layer of polyamide thin-film composite membranes. *J. Membr. Sci.* **2017**, *534*, 100−108.
(34) Tang, C. Y.; Kwon, Y.-N.; Leckie, J. O. Effect of membrane chemistry and coating layer on physiochemical properties of thin film composite polyamide RO and NF membranes: FTIR and XPS characterization of polyamide and coating layer chemistry. *Desalination* **2009**, *242*, 149−167 Journal Article.
(35) Esfahani, M. R.; Tyler, J. L.; Stretz, H. A.; Wells, M. J. M. Effects of a dual nanofiller, nano-TiO2 and MWCNT, for polysulfone-based nanocomposite membranes for water purification. *Desalination* **2015**, *372*, 47−56.
(36) Shen, J.; Liu, G.; Ji, Y.; Liu, Q.; Cheng, L.; Guan, K.; Zhang, M.; Liu, G.; Xiong, J.; Yang, J.; et al. 2D MXene Nanofilms with Tunable Gas Transport Channels. *Adv. Funct. Mater.* **2018**, *28*, 1801511.
(37) Chen, W.; Zhang, X.; Mamadiev, M.; Wang, Z. Sorption of perfluorooctane sulfonate and perfluorooctanoate on polyacrylonitrile fiber-derived activated carbon fibers: in comparison with activated carbon. *RSC Adv.* **2017**, *7*, 927−938.
(38) Malaki, M.; Maleki, A.; Varma, R. S. MXenes and ultrasonication. *J. Mater. Chem. A* **2019**, *7*, 10843−10857.
(39) Di Bartolomeo, A. Emerging 2D Materials and Their Van Der Waals Heterostructures. *Nanomaterials* **2020**, *10*, 579.
(40) Zhang, C. Interfacial assembly of two-dimensional MXenes. *J. Energy Chem.* **2021**, *60*, 417−434.
(41) Wang, X.; Li, Q.; Zhang, J.; Huang, H.; Wu, S.; Yang, Y. Novel thin-film reverse osmosis membrane with MXene Ti3C2T embedded in polyamide to enhance the water flux, anti-fouling and chlorine resistance for water desalination. *J. Membr. Sci.* **2020**, *603*, 118036.
(42) Hołda, A. K.; Vankelecom, I. F. J. Understanding and guiding the phase inversion process for synthesis of solvent resistant nanofiltration membranes. *J. Appl. Polym. Sci.* **2015**, *132*, DOI: 10.1002/app.42130.
(43) Grzebyk, K.; Armstrong, M. D.; Coronell, O. Accessing greater thickness and new morphology features in polyamide active layers of thin-film composite membranes by reducing restrictions in amine monomer supply. *J. Membr. Sci.* **2022**, *644*, 120112.
(44) Chai, G.-Y.; Krantz, W. B. Formation and characterization of polyamide membranes via interfacial polymerization. *J. Membr. Sci.* **1994**, *93*, 175−192.
(45) Freger, V.; Ramon, G. Z. Polyamide desalination membranes: Formation, structure, and properties. *Prog. Polym. Sci.* **2021**, *122*, 101451.
(46) Matthews, T. D.; Yan, H.; Cahill, D. G.; Coronell, O.; Mariñas, B. J. Growth dynamics of interfacially polymerized polyamide layers by diffuse reflectance spectroscopy and Rutherford backscattering spectrometry. *J. Membr. Sci.* **2013**, *429*, 71−80.
(47) Gohil, J. M.; Ray, P. A review on semi-aromatic polyamide TFC membranes prepared by interfacial polymerization: Potential for water treatment and desalination. *Sep. Purif. Technol.* **2017**, *181*, 159−182.
(48) Wu, X.; Ding, M.; Xu, H.; Yang, W.; Zhang, K.; Tian, H.; Wang, H.; Xie, Z. Scalable Ti3C2Tx MXene Interlayered Forward Osmosis Membranes for Enhanced Water Purification and Organic Solvent Recovery. *ACS Nano* **2020**, *14*, 9125−9135.
(49) Mokarizadeh, H.; Moayedfard, S.; Maleh, M. S.; Mohamed, S. I. G. P.; Nejati, S.; Esfahani, M. R. The role of support layer properties on the fabrication and performance of thin-film composite membranes: The significance of selective layer-support layer connectivity. *Sep. Purif. Technol.* **2021**, *278*, 119451.
(50) Ma, X.-H.; Yao, Z.-K.; Yang, Z.; Guo, H.; Xu, Z.-L.; Tang, C. Y.; Elimelech, M. Nanofoaming of Polyamide Desalination Mem-

branes To Tune Permeability and Selectivity. *Environ. Sci. Technol. Lett.* **2018**, *5*, 123−130.
(51) El-Arnaouty, M. B.; Abdel Ghaffar, A. M.; Eid, M.; Aboulfotouh, M. E.; Taher, N. H.; Soliman, E.-S. Nano-modification of polyamide thin film composite reverse osmosis membranes by radiation grafting. *J. Radiat. Res. Appl. Sci.* **2018**, *11*, 204−216.
(52) Farias-Aguilar, J. C.; Ramírez-Moreno, M. J.; Téllez-Jurado, L.; Balmori-Ramírez, H. Low pressure and low temperature synthesis of polyamide-6 (PA6) using Na 0 as catalyst. *Mater. Lett.* **2014**, *136*, 388−392.
(53) Li, H.; Shi, W.; Su, Y.; Zhang, H.; Qin, X. Preparation and characterization of carboxylated multiwalled carbon nanotube/polyamide composite nanofiltration membranes with improved performance. *J. Appl. Polym. Sci.* **2017**, *134*, 45268.
(54) Iqbal, M. A.; Tariq, A.; Zaheer, A.; Gul, S.; Ali, S. I.; Iqbal, M. Z.; Akinwande, D.; Rizwan, S. Ti3C2-MXene/Bismuth Ferrite Nanohybrids for Efficient Degradation of Organic Dyes and Colorless Pollutants. *ACS Omega* **2019**, *4*, 20530−20539.
(55) Shen, Z.; Chen, W.; Xu, H.; Yang, W.; Kong, Q.; Wang, A.; Ding, M.; Shang, J. Fabrication of a Novel Antifouling Polysulfone Membrane with in Situ Embedment of Mxene Nanosheets. *Int. J. Environ. Res. Publ. Health* **2019**, *16*, 4659.
(56) Li, H.; Shi, W.; Zhang, Y.; Du, Q.; Qin, X.; Su, Y. Improved performance of poly(piperazine amide) composite nanofiltration membranes by adding aluminum hydroxide nanospheres. *Sep. Purif. Technol.* **2016**, *166*, 240−251.
(57) Zhang, R.; Yu, S.; Shi, W.; Wang, X.; Cheng, J.; Zhang, Z.; Li, L.; Bao, X.; Zhang, B. Surface modification of piperazine-based nanofiltration membranes with serinol for enhanced antifouling properties in polymer flooding produced water treatment. *RSC Adv.* **2017**, *7*, 48904−48912.
(58) Qu, R.; Zeng, X.; Lin, L.; Zhang, G.; Liu, F.; Wang, C.; Ma, S.; Liu, C.; Miao, H.; Cao, L. Vertically-Oriented Ti3C2Tx MXene Membranes for High Performance of Electrokinetic Energy Conversion. *ACS Nano* **2020**, *14*, 16654−16662.
(59) Li, J.; Zheng, T.; Yuan, D.; Gao, C.; Liu, C. Probing the single and combined toxicity of PFOS and Cr(VI) to soil bacteria and the interaction mechanisms. *Chemosphere* **2020**, *249*, 126039.
(60) Tarlton, T.; Sullivan, E.; Brown, J.; Derosa, P. A. The role of agglomeration in the conductivity of carbon nanotube composites near percolation. *J. Appl. Phys.* **2017**, *121*, 085103.
(61) Li, S.; Leroy, P.; Heberling, F.; Devau, N.; Jougnot, D.; Chiaberge, C. Influence of surface conductivity on the apparent zeta potential of calcite. *J. Colloid Interface Sci.* **2016**, *468*, 262−275.
(62) Boffa, V.; Parmeggiani, L.; Nielsen, A. H.; Magnacca, G. Hydrophilicity and surface heterogeneity of TiO2-doped silica materials for membrane applications. *Microporous Mesoporous Mater.* **2016**, *221*, 81−90.
(63) Ismail, M. F.; Islam, M. A.; Khorshidi, B.; Tehrani-Bagha, A.; Sadrzadeh, M. Surface characterization of thin-film composite membranes using contact angle technique: Review of quantification strategies and applications. *Adv. Colloid Interface Sci.* **2022**, *299*, 102524.
(64) Wang, X.; Zhang, Q. Insight into the Influence of Surface Roughness on the Wettability of Apatite and Dolomite. *Minerals* **2020**, *10*, 114.
(65) Kang, Y.; Xia, Y.; Wang, H.; Zhang, X. 2D Laminar Membranes for Selective Water and Ion Transport. *Adv. Funct. Mater.* **2019**, *29*, 1902014.
(66) Cui, W.; Hu, Z.-Y.; Unocic, R. R.; Van Tendeloo, G.; Sang, X. Atomic defects, functional groups and properties in MXenes. *Chin. Chem. Lett.* **2021**, *32*, 339−344.
(67) Hermans, S.; Bernstein, R.; Volodin, A.; Vankelecom, I. F. J. Study of synthesis parameters and active layer morphology of interfacially polymerized polyamide−polysulfone membranes. *React. Funct. Polym.* **2015**, *86*, 199−208.
(68) Ren, C. E.; Alhabeb, M.; Byles, B. W.; Zhao, M.-Q.; Anasori, B.; Pomerantseva, E.; Mahmoud, K. A.; Gogotsi, Y. Voltage-Gated Ions Sieving through 2D MXene Ti3C2Tx Membranes. *ACS Appl. Nano Mater.* **2018**, *1*, 3644−3652.
(69) Pandey, R. P.; Rasheed, P. A.; Gomez, T.; Azam, R. S.; Mahmoud, K. A. A fouling-resistant mixed-matrix nanofiltration membrane based on covalently cross-linked Ti3C2TX (MXene)/cellulose acetate. *J. Membr. Sci.* **2020**, *607*, 118139.
(70) Wang, D.-X.; Su, M.; Yu, Z.-Y.; Wang, X.-L.; Ando, M.; Shintani, T. Separation performance of a nanofiltration membrane influenced by species and concentration of ions. *Desalination* **2005**, *175*, 219−225.

https://doi.org/10.1021/acsami.2c03796
ACS Appl. Mater. Interfaces 2022, 14, 25397−25408